

Periodic Projector Augmented Wave Density Functional Calculations on the Hexachlorobenzene Crystal and Comparison with the Experimental Multipolar Charge Density Model

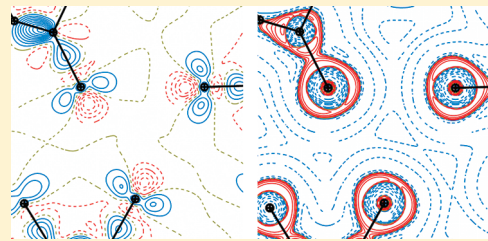
Emmanuel Aubert,[†] Sébastien Lebègue,[†] Martijn Marsman,[‡] Thai Thanh Thu Bui,[†] Christian Jelsch,[†] Slimane Dahaoui,[†] Enrique Espinosa,^{*,†} and János G. Ángyán^{*,†}

[†]CRM², UMR 7036, Institut Jean Barriol, Nancy University and CNRS, F-54506 Vandoeuvre-lès-Nancy, France

[‡]Fakultät für Physik and Center for Computational Materials Science, Universität Wien, Sensengasse 8/12, Wien 1090 Austria

 Supporting Information

ABSTRACT: The projector augmented wave (PAW) methodology has been used to calculate a high precision electron density distribution $\rho(\mathbf{r})$ for the hexachlorobenzene crystal phase. Implementing the calculation of the crystallographic structure factors in the VASP code has permitted one to obtain the theoretical multipolar $\rho(\mathbf{r})$. This electron density is compared with both the DFT electron density and the experimental multipolar model obtained from high-resolution X-ray diffraction data. This comparison has been carried out in intra- and intermolecular regions within the framework of the quantum theory of atoms-in-molecules (QTAIM) developed by Bader and co-workers. The characterization of the electron density in both C–Cl and Cl···Cl regions, as well as within the atomic basins, shows similar features for the three models. As a consequence, the observation of charge depletion and charge concentration regions around the halogen nuclei (along the C–Cl bonding axis and in the perpendicular plane, respectively) underlines the nature of halogen bonding in terms of electrophilic and nucleophilic interactions.



1. INTRODUCTION

In the experimental analysis of the electron density distribution $\rho(\mathbf{r})$ that is defined as the Fourier transform of the crystallographic X-ray structure factors, the goodness of the $\rho(\mathbf{r})$ function depends on several factors: (i) the completeness of the Fourier series (i.e., the maximum dimension of the reciprocal space vector to which the Fourier amplitudes have been measured), (ii) the quality of the Fourier amplitudes being derived from the measured Bragg diffraction intensities and (iii) the model used to describe the crystalline electron density distribution (which is straightforwardly involved in the phase problem of the structure factors). The accurate high-redundancy measure of low-temperature high-resolution X-ray Bragg intensities up to the maximum observed diffraction angle, along with the subsequent careful data reduction of the intensities data set, permits one to do the best with the experimental limitations associated with factors (i) and (ii). On the other hand, the use of multipolar models in (iii) has been demonstrated to significantly improve the structure factors phases with respect to those derived from the independent atoms model (IAM), used in classical structure determination, reproducing crystalline $\rho(\mathbf{r})$ features that result from intra- and intermolecular interactions.¹ Nevertheless, while the completeness of the Fourier series cannot be obviously recovered from experimental data, the quality of the structure factor amplitudes can be significantly affected by severe extinction and absorption effects, as well as for other possible phenomena

associated with crystal defects, beam homogeneity, instrumental instabilities, and so forth. In addition, even if multipolar atom models have been widely used for the modeling of crystalline $\rho(\mathbf{r})$ since the 70s,^{2,3} their limitations to fully describe the crystalline features have been also pointed out in some cases.^{4,5} Hence, to overcome intrinsic inaccuracies of the derived $\rho(\mathbf{r})$ model due to series truncation and other experimental effects, theoretical predictions can be very useful as a support for experimental charge density determination.^{6,7}

Ab initio total energy calculations using density functional theory (DFT) in the projector augmented wave⁸ (PAW) implementation has become a widespread tool for the structural study of a large range of materials.^{9–11} The Vienna Ab Initio Simulation Package (VASP) is one of the most popular computer codes¹² used by many research teams. One typical use of such calculations consists of completing missing or insufficiently resolved experimental data either of spectroscopic nature¹³ or those obtained from various diffraction experiments such as neutron, or more frequently, X-ray diffraction studies.¹⁴ Computationally established and approved models are particularly important in the interpretation of powder diffraction experiments, and they might also be necessary in resolving complicated diffraction patterns due to disorder phenomena in single crystal

Received: July 12, 2011

Revised: October 27, 2011

Published: October 31, 2011

studies. A largely unexploited aspect of PAW calculations implemented in the VASP program is the analysis of the calculated charge density.

In principle, the PAW method^{8,15} as an all-electron, frozen core approach, is able to provide accurate complete charge densities that can be compared with those obtained in high-resolution X-ray diffraction experiments, either directly, through the visualization of deformation density maps, or via the quantitative analysis of its topological features using the quantum theory of atoms-in-molecules (QTAIM) of Bader.¹⁶ In order to resolve complicated experimental situations, it might be necessary to simulate X-ray diffraction patterns directly from ab initio calculations, with a possible inclusion of dynamic effects. The VASP code offers now the necessary tools to perform such kinds of analyses, but these functionalities are relatively poorly documented for noninitiated users. Therefore, it might be interesting for a wider audience to present the formal background of these methods and to illustrate their usefulness on a relatively simple case and to point out a number of practical and technical aspects for conducting these charge density and X-ray diffraction studies according to the state of the art.

In the theoretical crystallographic community, the use of structure factors generated from electron densities obtained from ab initio or DFT calculations on isolated molecular systems or on periodic crystal models is quite common. As far as periodic calculations are concerned, most of these studies are being done either with the CRYSTAL code¹⁷ or by the all-electron FLAPW (full potential linearized augmented plane wave) Wien2k program.¹⁸ These programs have appropriate tools to generate structure factors.

The above-mentioned programs work with the all-electron wave function and give access, at any time, to the complete wave function (in a single determinant form). Meanwhile, an overwhelming majority of solid state electronic structure studies are done in a plane wave basis, where the use of either norm-conserving or ultrasoft pseudopotentials or a mixed-basis augmented plane wave methodology is mandatory. In the pseudopotential methods, one calculates a pseudo-valence wave function that has a simplified nodal structure with respect to the true valence wave function. In augmented plane wave approaches, it is possible to have the complete wave function (even the complete all-electron one) but the matching of the interstitial plane wave and of the atomic functions is limited in precision because of the high-order derivatives of the wave function, making uncertain the charge density derivatives on the atomic surfaces. Both of these difficulties are avoided in an elegant manner in the PAW approach, which allows one to determine the total, all-electron wave function (and charge density) with a computational cost comparable to that of an ultrasoft pseudopotential calculation.

As long as the complete charge density is represented either on a local basis set of Gaussian functions, or alternatively, on a regular grid, highly efficient computer programs are available to perform a QTAIM analysis according to the principles developed by Bader.¹⁶ Since, in the present work, we focus our attention on periodic solids, we mention only those Bader-integration tools, which are appropriate in these situations. In relation to the Gaussian-based CRYSTAL code,¹⁷ the Bader analysis can be performed with the TOPOND code developed by Gatti.¹⁹ Electron densities generated by the Wien2k code¹⁸ can be analyzed either with the AIM module of Wien2k or a separate program, Critic.²⁰

Another class of programs has been developed in the past 10 years, based on a discrete numerical representation of the electron density on a regular grid. The Integrity code²¹ uses a tricubic interpolation scheme in order to access the density and its analytical derivatives values between the grid points. This approach has the advantage that a detailed Bader analysis, including critical point and laplacian analyses, can also be performed. The program BADER developed by Henkelmann and co-workers²² is designed for the fast computation of atomic volumes and charges, based on a walking algorithm permitting to assign all grid points to one of the atomic basins of the system. Quite recently, Yu and Trinkle²³ proposed a more sophisticated version for this type of algorithm, which can be easily extended to nonregular grids as well. Another solution to the integration of the density and other properties within atomic volumes is given by the development of the QTREE method, which uses recursive subdivision of a symmetry-reduced wedge of the Wigner–Seitz cell, expressed as a union of tetrahedra.²⁴

One of the major difficulties is due to the fact that the topological properties are valid for the total (core + valence) charge density, which should be represented by a relatively high precision with continuous derivatives, at least to first and second orders. The requirement of having the total charge density makes the topological analysis on the results of pseudopotential calculations difficult, unless one succeeds in reconstructing an appropriate core density. The reconstruction is much more straightforward in PAW, where a well-defined prescription exists to have the true complete wave function (see the Computational Details section below).

In this work, periodic density functional calculations were carried out with the VASP code on the hexachlorobenzene (C_6Cl_6) crystal structure. Beyond the strong (intramolecular) and weak (intermolecular) interactions typically characterizing molecular crystals, this compound exhibits well-differentiated aromatic (C–C) and polarized (C–Cl) molecular bonds, as well as Cl···Cl halogen bonding interactions of main interest in crystal engineering. Hexachlorobenzene is a good compromise between the diversity of bonding interactions and the simplicity of the unit-cell composition, being therefore a nice target material to apply VASP periodic calculations (it is noticed that chlorine···chlorine interactions involved in other crystal structures were also studied with other codes^{25,26}). To fully compare with standard experimental procedures, the theoretical charge density model $\rho(\mathbf{r})$ of crystalline C_6Cl_6 is derived from the theoretical structure factors issued from the calculated wave function. Hence, the theoretical $\rho(\mathbf{r})$ is described in terms of the superposition of atomic contributions based on multipolar expansion terms centered at nuclei (Hansen and Coppens multipolar model³) and fitted against the structure factors data set. The same procedure has also been used to obtain the crystalline $\rho(\mathbf{r})$ model of C_6Cl_6 , accurately derived from previously measured low-temperature high-resolution X-ray diffraction data.²⁷ Thus, both the theoretically calculated and the experimentally determined $\rho(\mathbf{r})$ models are here compared to the periodic calculations undertaken with VASP. This study is carried out within the framework of QTAIM, comparing the integrated and local bond critical point topological properties of the three models.

2. COMPUTATIONAL DETAILS

2.1. Complete Electronic Charge Density in the PAW Formulation.

Following the general decomposition procedure

of any operator expectation value in the PAW scheme,^{8,15} the electron density becomes

$$n(r) = \tilde{n}(r) + \sum_R (n_R^1(r) - \tilde{n}_R^1(r))$$

where the pseudodensity $\tilde{n}(r)$ is evaluated on a regular grid in the whole (periodic) cell, while $\tilde{n}_R^1(r)$ and $n_R^1(r)$ are calculated on a radial grid centered around each R -atom and comprised within a region called the augmentation sphere. This decomposition applies to both valence and core electrons. Since this formula involves a density on a regular grid and two densities on radial grids, the contributions represented on the radial grids have to be added onto the regular grid using a polynomial interpolation scheme. In contrast to standard pseudopotential methods in which only the $\tilde{n}(r)$ term is available, the complete density is recovered within the PAW method. We recall that the above-defined complete density corresponds to the true wave function of the system, which has a full nodal structure everywhere in space, in contrast to the pseudo-wave function, which matches the true wave function only outside of the atomic augmentation spheres. The reconstitution of the valence density using the formula above is crucial for performing meaningful charge density analyses and is needed to evaluate theoretical electronic structure factors, corresponding to the quantities measured in X-ray diffraction experiments.

2.2. Electronic Structure Calculations by VASP. Periodic DFT calculations have been performed using the VASP code.^{28–30,12} The Kohn–Sham equations have been solved in a plane-wave basis set using the PAW method of Blöchl.^{8,15} We have used the exchange-correlation functional of Perdew, Burke, and Ernzerhof³¹ (PBE) based on the generalized gradient approximation (GGA). We also tried a hybrid functional such as that of Heyd, Scuseria, and Ernzerhof (HSE),³² but the calculation failed to converge (any amount of Hartree–Fock exchange leads to nonconverging calculations, and even a pure Hartree–Fock calculation fails). The wave function and the density in the augmentation spheres were described by standard PBE PAW atomic data sets. The plane wave cutoff of the calculation was set to a relatively high value (900 eV) in order to ensure convergence. Experimental cell parameters ($a = 7.9724(2)$ Å, $b = 3.7626(2)$ Å, $c = 14.6851(2)$ Å, and $\beta = 92.456(1)$ ° at $T = 100(2)$ K) and atomic coordinates obtained from the experimental charge density refinements were used as input for the VASP calculation and were not optimized. A reasonably dense sampling of the Brillouin zone has been ensured with a k -point mesh of (8, 16, 4). The electron density is represented on a regular grid comprising $240 \times 120 \times 432$ points along the crystallographic axes. This real space sampling is 1.5 times denser than the default grid associated with the 900 eV energy cutoff. By switching on the keyword LAECHG in the input file, any VASP user can obtain three files named AECCAR0, AECCAR1, and AECCAR2. The file AECCAR0 contains the core density, AECCAR1 corresponds to the promolecular density (i.e. the superposition of spherical atomic densities), and AECCAR2 contains the valence density. For all these files, the quantities are encoded on a regular grid. The structure factors are calculated from the full valence electron density. To perform the calculations of the structure factors, a cutoff parameter (keyword ENCUTAE) must be given in the input file INCAR which controls the resolution in the reciprocal space (i.e., the maximum size of the reciprocal space vector) and therefore the total number of structure factors that are calculated within full completeness.

Finally, some caution is needed when using the AECCAR0 file since it contains the core density on a regular grid instead of the atom-centered grids. As a consequence, it might not integrate exactly to the expected number of core electrons.

2.3. Multipole Refinement. Multipolar refinements were performed with the MoPro suite of programs, including the VMoPro tool for the topological analysis of the charge density.^{33,34} The multipolar refinement against the theoretically calculated structure factors was initiated starting with the atomic positions obtained at the converged experimental multipolar model. Valence electron distributions for chlorine and carbon atoms were similarly described in the fitting against either experimental or theoretical structure factors. Accordingly, the Slater-type radial functions were expanded up to the hexadecapolar level ($l = 4$) for chlorine atoms (n_l , ζ : 4,4,6,8 for $l = 1,2,3,4$; 4.4 bohr⁻¹) and up to octupolar level ($l = 3$) for carbon atoms (n_l , ζ : 2,2,3 for $l = 1,2,3$; 3.0 bohr⁻¹) in both cases. In the fitting against theoretical data, core electrons were omitted from MoPro atomic definitions, since the VASP structure factors correspond to valence electrons only.

Theoretical and experimental refinements were done against structure factor modulii, minimizing the numerator of

$$wR_2F = \sqrt{\frac{\sum \frac{1}{\sigma^2(F_{\text{obs}})} \left(\frac{1}{k} |F_{\text{obs}}| - |F_{\text{calc}}| \right)^2}{\sum \frac{1}{\sigma^2(F_{\text{obs}})} \left(\frac{1}{k} |F_{\text{obs}}| \right)^2}}$$

where $|F_{\text{obs}}|$ and $|F_{\text{calc}}|$ are the observed (either theoretically calculated with VASP or experimentally determined) and the calculated (by the multipolar model) structure factor modulii, k is the scale factor, and $\sigma(F_{\text{obs}})$ is the standard deviation, which was set to unity for each theoretical structure factor. As the structure factors were computed with VASP on the same scale as those calculated from the multipolar model with MoPro, the scale factor parameter (k) of the multipolar model was thus fixed to unity in the refinement against theoretical data. The quality of the experimental refinement was also judged from the goodness of fit (g.o.f.) value

$$\text{g.o.f.} = \sqrt{\frac{\sum \frac{1}{\sigma^2(F_{\text{obs}})} \left(\frac{1}{k} |F_{\text{obs}}| - |F_{\text{cqlc}}| \right)^2}{n_{\text{obs}} - n_{\text{par}}}}$$

where n_{obs} and n_{par} are the number of the structure factors and the number of parameters used for the multipolar refinement, respectively. For the theoretical model, atomic displacement parameters were fixed to zero since thermal smearing is not convoluted to the fundamental state of the electron density distribution in the structure factor calculation carried out by VASP.

2.4. Topological Analysis of the Charge Density. The critical points (CPs) between bonded and interacting atoms in the experimental and theoretical charge densities were searched with the VMoPro module of the MoPro software.³³ The CP position between a pair of atoms is found by minimizing the gradient norm of the total electron density, starting from the middle position between them. At first, the minimization is done in one dimension on the segment between the two nuclei, then a three-dimensional steepest descent is carried out.

In this procedure, the topological properties such as the laplacian and the Hessian matrix at CP are obtained by Taylor formulas developed up to sixth order. Initially, an orthonormal basis ($\mathbf{e}_1, \mathbf{e}_2, \mathbf{e}_3$) is defined with associated coordinates (x_1, x_2, x_3). Then, at a given \mathbf{r} position ($\mathbf{r} = \sum x_i \cdot \mathbf{e}_i$), the numerical second derivative of the f function (either the electron density or the electrostatic potential) along the unitary \mathbf{e}_k -vector direction is obtained by

$$\partial^2 f / \partial x_k^2 = [270D_{1,k} - 27D_{2,k} + 2D_{3,k}] / 180 + o(u^6)$$

where $D_{i,k} = [f(\mathbf{r} + i \cdot u \cdot \mathbf{e}_k) + f(\mathbf{r} - i \cdot u \cdot \mathbf{e}_k) - 2f(\mathbf{r})] / u^2$ for $i = 1, 2, 3$ and u is a small increment.

The cross derivatives with respect to the directions of two orthogonal vectors \mathbf{e}_j and \mathbf{e}_k are calculated as

$$\partial^2 f / \partial x_j \partial x_k = (270G_{1,j,k} - 27G_{2,j,k} + G_{3,j,k}) / 720 + o(u^6)$$

where $G_{i,j,k} = [f(\mathbf{r} - i \cdot u(\mathbf{e}_j + \mathbf{e}_k)) + f(\mathbf{r} + i \cdot u(\mathbf{e}_j + \mathbf{e}_k)) - f(\mathbf{r} + i \cdot u(-\mathbf{e}_j + \mathbf{e}_k)) - f(\mathbf{r} + i \cdot u(\mathbf{e}_j - \mathbf{e}_k))] / u^2$ for $i = 1, 2, 3$.

These differential expressions using small u -increments in the range 10^{-5} to 10^{-4} Å lead to reliable and stable numerical results, which do not depend on the orientation of the orthonormal basis ($\mathbf{e}_1, \mathbf{e}_2, \mathbf{e}_3$).

Also, since the calculation of atomic dipoles and quadrupoles was not available in the BADER code²² used to calculate the integrated topological properties, we have implemented these features, which are now included in the official distribution of the BADER code. For a given Bader basin Ω_K belonging to an atom K of coordinates R^K_α , the corresponding atomic dipole D^K_α along a Cartesian component α is calculated in the following way:

$$D^K_\alpha = \int_{\Omega_K} \rho(\mathbf{r}) \cdot (r_\alpha - R^K_\alpha) \cdot d^3r$$

while the quadrupole $Q^K_{\alpha\beta}$ tensor is calculated as:

$$Q^K_{\alpha\beta} = \frac{1}{2} \int_{\Omega_K} \rho(\mathbf{r}) \cdot (3(r_\alpha - R^K_\alpha)(r_\beta - R^K_\beta) - \delta_{\alpha\beta}|\mathbf{r} - \mathbf{R}^K|^2) \cdot d^3r$$

following Buckingham's widely accepted definition.³⁵ Our implementation was tested by comparing the atomic quadrupole moment components for an isolated hexachlorobenzene molecule with the ones obtained with the AIMAll program,³⁶ which uses the output of a Gaussian03³⁷ calculation. The results were identical, within 0.03 e· a_0^2 , therefore validating our implementation (see Supporting Information for details; caution should be taken in such comparison since quadrupole definitions in both programs differ by a factor of 1/2). Also, we have reconstructed the molecular quadrupole moments from atomic charges, dipoles, and quadrupoles and compared the results with the quadrupole moment obtained as the quantum mechanical expectation value from the output of the Gaussian03 calculation. The agreement was reasonable within errors due to the grid and to the integration algorithm (maximum discrepancy of 0.2 e· a_0^2 , i.e., 12% for the largest quadrupolar tensor component). Finally, we have added a condition taking into account the periodicity of the crystal, so that densities generated with VASP can be treated with this approach. More details can be found in the Supporting Information.

3. RESULTS AND DISCUSSIONS

3.1. The Experimental Multipolar Model. Hexachlorobenzene crystallizes in the monoclinic system ($P2_1/n$ space group).

Table 1. Integrated Topological Atomic Volumes (V), Charges (q), Dipole Moment (μ) and Eigenvalues of the Traceless Atomic Quadrupolar Tensor (Q_{ii})^a

atom	V (Å ³)	q (e)	μ (e· a_0)	Q_{aa} (e· a_0^2)	$Q_{\beta\beta}$ (e· a_0^2)	$Q_{\gamma\gamma}$ (e· a_0^2)
C1	8.79	0.13	0.091	-2.96	1.37	1.59
	8.90	0.14	0.102	-2.89	1.29	1.60
	8.75	0.14	0.148	-2.71	1.21	1.50
C2	9.06	0.01	0.112	-3.09	1.36	1.73
	8.85	0.15	0.111	-2.87	1.29	1.58
	8.74	0.14	0.158	-2.71	1.21	1.50
C3	9.07	0.04	0.060	-2.84	1.18	1.66
	8.92	0.15	0.115	-2.87	1.33	1.54
	8.80	0.16	0.144	-2.75	1.25	1.50
Cl1	28.08	-0.08	0.314	-1.65	-1.27	2.92
	28.16	-0.14	0.297	-1.74	-1.08	2.82
	28.38	-0.15	0.078	-1.77	-1.32	3.10
Cl2	27.42	-0.03	0.254	-1.89	-1.28	3.18
	27.65	-0.15	0.286	-1.73	-1.04	2.76
	27.72	-0.14	0.067	-1.76	-1.32	3.07
Cl3	27.60	-0.08	0.295	-1.61	-1.51	3.13
	27.54	-0.15	0.297	-1.70	-0.97	2.68
	27.63	-0.15	0.075	-1.73	-1.28	3.01
C ₆ Cl ₆	220.05			-2.89	0.83	2.06
	220.05			-3.99	-2.74	6.74
	220.05			-1.55	1.21	0.34

^a Results from the multipolar refinements against experimental and theoretical data at experimental geometry are given in upper and middle lines, respectively. Corresponding values issued from the Vasp electron density, directly derived from the wave function, are given in lower lines.

The asymmetric unit is formed by a half of the molecule, the second half being generated by an inversion center located in the middle of the aromatic ring. A former experimental multipolar $\rho(\mathbf{r})$ model of hexachlorobenzene was determined by our group with chlorine atoms described by the most relevant multipolar terms only, namely two quadrupoles and two octupoles.²⁷ To undertake the most complete comparison with the theoretical model, we have decided to extend the description of chlorine atoms to all the multipolar terms up to hexadecapolar level. Therefore, a new experimental $\rho(\mathbf{r})$ model has been fitted against the same set of experimental structure factors, by using the unit cell parameters previously reported. At convergence, the new $\rho(\mathbf{r})$ model has been characterized in terms of QTAIM topological analysis. The integrated properties within the atomic basins are gathered in Table 1, and local properties at bond critical points observed in intramolecular and intermolecular regions are shown in Tables 2 and 3, respectively. In addition, residual (Figure 1d), deformation (Figures 2d,e,f and 4b) and laplacian (Figures 3b and 4d) maps have been also generated to compare with theoretical results. As expected, only very small differences appear between the present and the previously reported experimental $\rho(\mathbf{r})$ model, as shown by the comparison of topological parameters at bond critical points in intra- and intermolecular regions and of residual, deformation, and laplacian maps (from ref 27, the topological values at the intramolecular bond critical points range: $\rho_{C-Cl} = 1.38-1.42$ e·Å⁻³ and $\rho_{C-C} = 2.08-2.10$ e·Å⁻³; $\nabla^2 \rho_{C-Cl} = -2.5$ to -3.5 e·Å⁻⁵ and $\nabla^2 \rho_{C-C} = -17.3$ to -18.5 e·Å⁻⁵, while for the intermolecular Cl···Cl interactions the ranges are $\rho_{Cl-Cl} = 0.03-0.06$ e·Å⁻³ and $\nabla^2 \rho_{Cl-Cl} = 0.3-0.6$ e·Å⁻⁵).

Table 2. Topological Properties of $\rho(r)$ at Intramolecular Bond (3,−1) and Ring (3,+1) Critical Points of the Hexachlorobenzene Molecule^a

	$d_{\text{At1-cp}}$ (Å)	$d_{\text{cp-At2}}$ (Å)	ρ (e·Å ^{−3})	$\nabla^2 \rho$ (e·Å ^{−5})	λ_1 (e·Å ^{−5})	λ_2 (e·Å ^{−5})	λ_3 (e·Å ^{−5})	ε
C ₁ −C ₂	0.6988	0.7033	2.07	−16.7	−16.3	−12.6	12.2	0.23
	0.7046	0.6976	2.02	−15.5	−15.0	−12.0	11.5	0.20
	0.700	0.702	2.10	−24.9	−16.1	−13.7	5.0	0.17
C ₂ −C ₃	0.7023	0.7005	2.09	−17.4	−16.5	−12.9	12.0	0.22
	0.7015	0.7012	2.01	−15.6	−14.9	−12.1	11.4	0.19
	0.706	0.696	2.10	−29.0	−17.8	−14.7	3.5	0.21
C ₁ −C ₃	0.6804	0.7208	2.08	−18.1	−16.6	−12.9	11.4	0.22
	0.7005	0.7000	2.02	−15.9	−15.1	−12.1	11.3	0.20
	0.699	0.701	2.10	−21.4	−14.7	−12.5	5.8	0.17
C ₁ −Cl ₁	0.7800	0.9349	1.41	−3.9	−7.70	−7.7	11.5	0.00
	0.7522	0.9627	1.38	−3.5	−8.0	−7.3	11.8	0.08
	0.734	0.981	1.46	−8.4	−8.8	−8.3	8.7	0.07
C ₂ −Cl ₂	0.7733	0.9386	1.44	−3.9	−8.4	−7.4	11.9	0.12
	0.7471	0.9641	1.39	−3.6	−8.0	−7.4	11.8	0.08
	0.733	0.978	1.47	−9.0	−8.8	−8.2	8.1	0.08
C ₃ −Cl ₃	0.7878	0.9261	1.42	−4.2	−8.1	−7.3	11.2	0.10
	0.7490	0.9646	1.39	−3.6	−8.1	−7.3	11.7	0.10
	0.732	0.981	1.46	−7.3	−8.6	−7.9	9.1	0.09
ring	1.4016	1.4018	0.16	3.9	−0.2	1.4	1.8	0.24
	1.4017	1.4017	0.13	3.4	−0.2	1.8	1.8	0.01
	1.401	1.401	0.16	3.2	−0.4	1.8	1.8	0.01

^a Results obtained from the multipolar refinement against experimental and theoretical data at the experimental geometry are given in upper and middle lines, respectively. Corresponding values issued from the VASP electron density, directly derived from the wave function, are given in lower lines.

3.2. Theoretical Structure Factors and Refinement. *3.2.1. C_6Cl_6 Static Structure Factors.* The structure factors calculated by VASP are in Cartesian form and correspond to the 132 valence electrons of the unit cell. As the crystal structure of C_6Cl_6 is centro-symmetric with the origin chosen on an inversion center, the imaginary components of these structure factors must be strictly zero. Indeed, the largest numerical value obtained for the latter is $\sim 4 \times 10^{-12}$, showing the good quality of the algorithm used. Similarly, the $F(000)$ coefficient (which corresponds to the total number of valence electron in the unit cell) integrated to 132.00, showing no discrepancy compared to the expected value. Prior to the multipolar refinement, these structure factors were converted in moduli, and only the crystallographic unique reflections were kept, the sorting being performed with the Sortav program.³⁸ At the end of this process, the data set contained 3663 unique structure factors, corresponding to full completeness up to a reciprocal resolution of 1.0 Å^{−1}. This maximal resolution is the same as the limit used in the experimental study and allows the deconvolution of thermal and deformation effects when dynamical structure factors are considered. The uncertainties on these structure factors, represented by $\sigma(F_{\text{obs}})$ values and required for the multipolar refinement, were set to unity as explained in section 2.3.

The multipolar model fitted against the theoretical structure factors converged to the agreement factor $wR_2F = 0.0357$, while the IAM, defined as the addition of spherical atomic densities centered at the atomic positions and obtained prior to the multipolar refinement, was converged to $wR_2F = 0.1102$. The residual electron density map (Figure 1a) shows peaks centered at the chlorine nuclei (~ 0.40 e·Å^{−3}) and smaller features along the C–Cl bonds. These trends, which correspond to the valence electron density and that are not taken into account by the multipolar atom model, appear predominantly at high resolution,

since the residual map drawn up to 0.7 Å^{−1} resolution displays significantly lowered residual density (0.15 e·Å^{−3} located at the Cl nuclei, see Figure 1b). The refinement of atomic positions does not lead to any further decrease in the residual densities, and the wR_2F factor is only marginally better ($wR_2F = 0.0351$). Hence, the model retained for the following analysis of the charge density corresponds to that where atomic positions are fixed to experimental values.

The static deformation density maps in the hexachlorobenzene molecular plane calculated from the refinement against theoretical and measured structure factors are very similar. The regions along the C–Cl bond directions at both sides of the chlorine nuclei exhibit depleted electron density distributions, while a more or less structured positive charge density region is observed in the plane perpendicular to the bond axis direction (Figure 2a,d). The carbon–chlorine bonds are polarized, with a build-up of charge density close to the C-atoms and a depletion in the proximity of Cl atoms. In the theoretical model, very similar torus-shaped regions of charge accumulation around the three crystallographic independent halogen atoms are observed (Figures 2b,c, 3a,c, and 4a). Conversely, the experimental refinement leads to more dissymmetric electron density distributions around these halogen atoms (Figures 2d,e,f, 3b, and 4b), while keeping the same relative orientations of charge concentration (CC) and charge depletion (CD) regions. In spite of these dissymmetric densities, the laplacian maps compare very well within the three-center halogen···halogen interactions plane (Figure 4c,d). Indeed, as observed in the experimental charge density, the theoretical model displays CC and CD zones in the valence shell charge concentration (VSCC) regions of the chlorine atoms. These areas correspond to nucleophilic and electrophilic sites around the halogen nuclei, as a consequence of

Table 3. Topological Properties of $\rho(r)$ at the Intermolecular Bond Critical Points of the Hexachlorobenzene Crystal Structure^a

Interaction	d (Å)	ρ (e·Å ⁻³)	$\nabla^2 \rho$ (e·Å ⁻⁵)	λ_1 (e·Å ⁻⁵)	λ_2 (e·Å ⁻⁵)	λ_3 (e·Å ⁻⁵)
$\text{Cl}_1^{\text{i}} \cdots \text{Cl}_2^{\text{ii}}$	3.4466(1)	0.049	0.62	-0.09	-0.08	0.80
		0.055	0.60	-0.13	-0.13	0.87
		0.045	0.59	-0.10	-0.10	0.78
$\text{Cl}_2^{\text{i}} \cdots \text{Cl}_3^{\text{iii}}$	3.4701(1)	0.057	0.57	-0.15	-0.14	0.87
		0.053	0.59	-0.12	-0.12	0.83
		0.041	0.56	-0.09	-0.09	0.74
$\text{Cl}_3^{\text{i}} \cdots \text{Cl}_1^{\text{iv}}$	3.6662(1)	0.038	0.41	-0.09	-0.09	0.59
		0.035	0.40	-0.08	-0.08	0.56
		0.028	0.38	-0.05	-0.05	0.48
$\text{Cl}_1^{\text{i}} \cdots \text{Cl}_1^{\text{v}}$	3.8221(2)	0.029	0.35	-0.06	-0.05	0.46
		0.025	0.32	-0.05	-0.05	0.42
		0.026	0.31	-0.05	-0.04	0.40
$\text{Cl}_2^{\text{i}} \cdots \text{Cl}_2^{\text{iii}}$	3.6238(2)	0.040	0.50	-0.10	-0.06	0.66
		0.037	0.47	-0.08	-0.08	0.63
		0.037	0.45	-0.08	-0.08	0.61
$\text{Cl}_3^{\text{i}} \cdots \text{Cl}_3^{\text{vi}}$	3.6355(2)	0.035	0.47	-0.06	-0.05	0.59
		0.037	0.46	-0.08	-0.07	0.61
		0.036	0.44	-0.08	-0.07	0.60
$\text{Cl}_2^{\text{i}} \cdots \text{Cl}_2^{\text{vii}}$	3.7626(2)	0.031	0.36	-0.07	-0.06	0.50
		0.031	0.37	-0.07	-0.06	0.50
		0.031	0.36	-0.07	-0.06	0.49
$\text{Cl}_3^{\text{i}} \cdots \text{Cl}_3^{\text{vii}}$	3.7626(2)	0.032	0.36	-0.08	-0.07	0.51
		0.033	0.40	-0.07	-0.02	0.48
		0.032	0.39	-0.06	-0.03	0.48
$\text{C}_1^{\text{i}} \cdots \text{Cl}_1^{\text{viii}}$	3.5081(4)	0.043	0.47	-0.06	-0.04	0.58
		0.040	0.47	-0.07	-0.04	0.57
		0.038	0.45	-0.07	-0.04	0.57
$\text{C}_2^{\text{i}} \cdots \text{Cl}_1^{\text{viii}}$	3.6774(4)	0.043	0.47	-0.06	-0.04	0.58
		0.040	0.47	-0.07	-0.04	0.57
		0.038	0.45	-0.07	-0.04	0.57
$\text{C}_2^{\text{i}} \cdots \text{Cl}_3^{\text{vii}}$	3.6673(4)	0.037	0.41	-0.04	0.00	0.45
		0.034	0.40	-0.05	-0.01	0.46
		0.032	0.39	-0.05	-0.01	0.46
$\text{C}_2^{\text{i}} \cdots \text{C}_3^{\text{vii}}$	3.4751(6)	0.039	0.42	-0.05	-0.02	0.48
		0.034	0.39	-0.04	-0.01	0.44
		0.032	0.36	-0.05	-0.02	0.43

^a Results obtained from the multipolar refinement against experimental and theoretical data at the experimental geometry are given in upper and middle lines, respectively. Corresponding values issued from the VASP electron density, directly derived from the wave function, are given in lower lines. For comparison purposes between the models, the topological properties are shown with a larger number of significant digits than that expected from the estimated standard deviations. Symmetry codes: *i*: x, y, z ; *ii*: $1/2 - x, -1/2 + y, 1/2 - z$; *iii*: $-1/2 - x, -1/2, 1/2 - z$; *iv*: $-1 + x, 1 + y, z$; *v*: $1/2 - x, 1/2 + y, 1/2 - z$; *vi*: $-1 - x, 2 - y, -z$; *vii*: $x, -1 + y, z$; *viii*: $x, 1 + y, z$.

the polar flattening effect.²⁷ From their positions within the synthon (Figure 4), CC and CD regions face each other along the three edges of this structural motif, indicating attractive electrophilic···nucleophilic interactions. Another difference concerns the magnitude of the deformation electron density. Thus, whereas its value reaches ca. $+0.25 \text{ e} \cdot \text{\AA}^{-3} / -0.20 \text{ e} \cdot \text{\AA}^{-3}$ along the C–Cl bond direction of the experimental model, these quantities are lowered when VASP structure factors are used for the multipolar refinement ($+0.15 \text{ e} \cdot \text{\AA}^{-3} / -0.10 \text{ e} \cdot \text{\AA}^{-3}$).

3.2.2. C_6Cl_6 Dynamic Structure Factors. In order to have a deeper insight on the almost spherical residual electron densities located on the halogen atoms (Figure 1), a dynamic electron density distribution was generated. With the aim of minimizing

correlations between multipolar and atomic displacement parameters (ADPs) during the subsequent refinement, static structure factors corresponding to the valence electron density were first added to the structure factors corresponding to the static atomic cores. These latter were calculated with the MoPro software, using the experimental C_6Cl_6 crystal structure. It is noteworthy that the VASP core density was not used in order to avoid an expected imprecision due to the rapidly varying shape of the density close to the nuclei. In that way, a Debye–Waller term ($\text{DW}(\sin \theta / \lambda) = \exp[-8\pi^2 U_{\text{iso}}(\sin \theta / \lambda)^2]$) was multiplied by the total (valence plus core) static structure factors, leading to a dynamic electron density in direct space involving all the electrons. For the purpose of comparison, the isotropic atomic

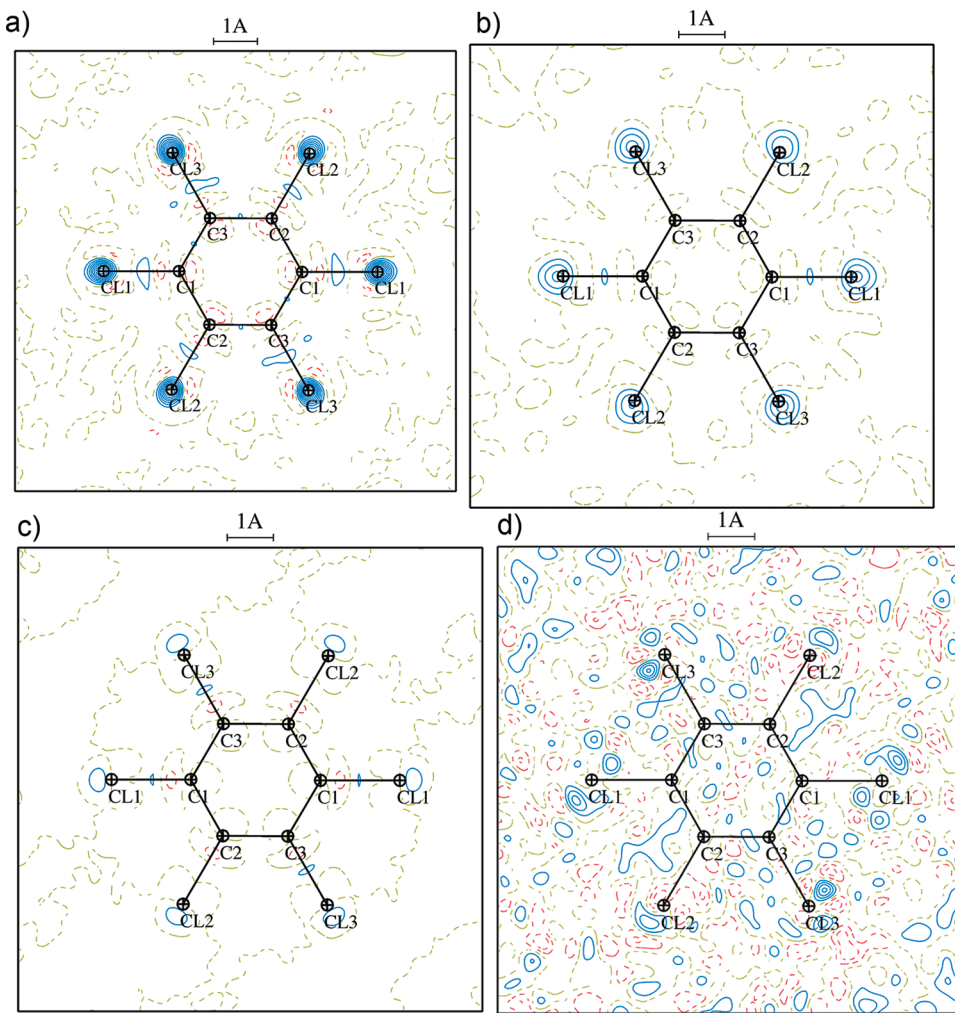


Figure 1. Theoretical residual electron density maps within the $\text{Cl}_1-\text{C}_1-\text{C}_2$ plane, calculated with static structure factors up to a resolution of (a) $\sin \theta/\lambda < 1 \text{ \AA}^{-1}$ and (b) $\sin \theta/\lambda < 0.7 \text{ \AA}^{-1}$, and dynamical structure factors up to a resolution of (c) $\sin \theta/\lambda < 1 \text{ \AA}^{-1}$ (corresponding to the multipolar model where ADPs were refined together with all the other multipolar parameters). (d) Experimental residual map calculated up to $\sin \theta/\lambda < 1 \text{ \AA}^{-1}$ resolution. Contour intervals at $0.05 \text{ e} \cdot \text{\AA}^{-3}$ level; positive, negative, and zero contours are in solid blue and dashed red and green lines, respectively.

displacement parameter used in the Debye–Waller term ($U_{\text{iso}} = 0.015 \text{ \AA}^2$) was chosen close to the average of the equivalent isotropic atomic displacement parameters obtained in the experimental data modeling ($\langle U_{\text{iso}} \rangle = 0.011 \text{ \AA}^2$ and 0.015 \AA^2 for C and Cl atoms, respectively).

The residual density maps obtained at the end of the multipolar refinement, where ADPs were kept fixed to 0.015 \AA^2 , are similar to those obtained from the static structure factors (Figure S3), the residual densities centered at the chlorine nuclei being $\sim 0.20–0.25 \text{ \AA}^{-3}$. Thus, the convolution itself of the static charge density with the dynamic probability density distribution does not allow the parameters of the multipolar atom model to take these residues into account.

However, the refinement of atomic ADPs, together with the multipolar parameters, leads to a drastic diminution of the residual densities, as previously observed in the case of diamond.³⁹ The largest residual densities ($\sim 0.05 \text{ e} \cdot \text{\AA}^{-3}$) are actually located very close to the chlorine nuclei ($\sim 0.4 \text{ \AA}$) in the C–Cl bond direction (Figure 1c). Since the region of interest for the characterization of intermolecular interactions (the σ -hole

involved in halogen···halogen interactions) is located in this region but at $\sim 0.7 \text{ \AA}$ from the chlorine nuclei (Figure 2a, 3a), such residual densities certainly do not affect the topological description of halogen···halogen interactions. In this model, the individual ADPs were refined to mean values of 0.01497 \AA^2 and of 0.01493 \AA^2 for carbon and chlorine atoms, respectively. The deviation of the chlorine atoms ADPs from the value imposed on the Debye–Waller term is lower than 3 times the estimated standard deviation obtained at the end of the multipolar refinement of the experimental data ($\langle \sigma \rangle = 3 \times 10^{-5} \text{ \AA}^2$).

The observed atom-centered residual densities (Figure 1) are due to the different radial dependences between the electron densities calculated from VASP and from the multipolar model. Indeed, whereas in the former, superposition of plane waves and atom-centered numerical radial functions are used, Slater-type functions define the radial dependences in the latter, leading to different shapes of the electron density functions. The use of a higher energy cutoff (900 eV; see section 2.2), well beyond the limit of the resolution used in the refinement (1.0 \AA^{-1}), excluded an eventual problem with Fourier truncation effects.

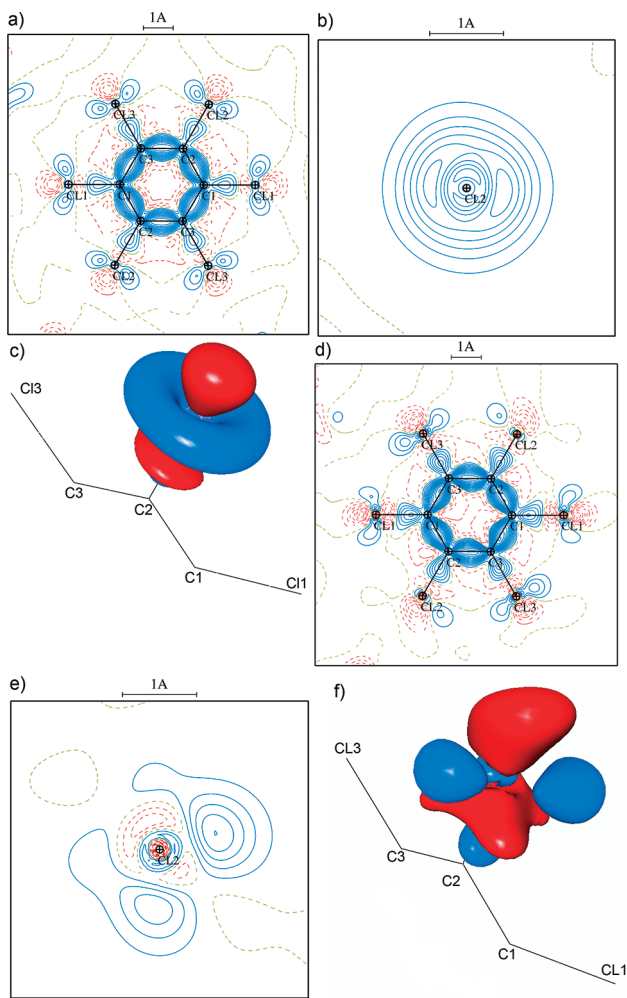


Figure 2. Static deformation density maps of the theoretical multipolar model: (a) $\text{Cl}1-\text{C}1-\text{C}2$ plane. Contour intervals are at $0.05\text{e}\cdot\text{\AA}^{-3}$ level and are defined as in Figure 1. (b) Plane perpendicular to the $\text{C}2-\text{Cl}2$ bond at 0.1\AA from the $\text{Cl}2$ -nucleus, corresponding to the maximum of the deformation density at the chlorine atom. Contour intervals are at $0.025\text{ e}\cdot\text{\AA}^{-3}$ level and are defined as in Figure 1. (c) Isosurfaces ($\pm 0.05\text{e}\cdot\text{\AA}^{-3}$) around the $\text{Cl}2$ -atom. Positive and negative values are represented in red and blue colors, respectively. Static deformation density maps of the experimental multipolar model: (d) $\text{Cl}1-\text{C}1-\text{C}2$ plane (same contours as for panel a) and (e) plane perpendicular to the $\text{C}2-\text{Cl}2$ bond at 0.1\AA from the $\text{Cl}2$ -nucleus, corresponding to the maximum of the deformation density at the chlorine atom (same contours as for panel b). (f) Isosurfaces ($\pm 0.05\text{e}\cdot\text{\AA}^{-3}$) around the $\text{Cl}2$ -atom, with the same color scheme as for panel c.

3.3. Topological Analyses of Calculated Charge Densities. The atomic volumes, charges, dipoles, and quadrupoles were integrated by using the modified BADER software from the Henkelman group, which uses electron densities projected on grids.²² Experimental and theoretical multipolar valence electron densities were then sampled with the same grid as the one used in the VASP calculation (see section 2.2), and total (core + valence) densities were used to define atomic basins. Such procedure ensures the best results when integrations on grids are carried out. Table 1 shows integrated topological properties for both experimental and theoretical multipolar models, along with the corresponding values obtained from the direct analysis of the VASP density (i.e., straightforwardly derived from the wave

function and projected on the grid). Atomic volumes were found to be very similar for the multipolar and the VASP densities. The experimental integrated charges are smaller in magnitude than the theoretical values but display a wider dispersion. The use of the multipolar model shows little influence on this property when compared to the results issued from the wave function. For all models, it should be pointed out, however, that all chlorine atoms display a small negative charge, counterbalanced by positively charged carbon atoms. The theoretically calculated intramolecular charge transfer from carbon to chlorine is, however, overestimated in comparison to the result of the experimental multipolar fitting. Whereas the assessment of a standard deviation on the integrated charge is intrinsically difficult, it should be noted that the average standard deviations on the electron valence populations obtained in the experimental multipolar model are 0.09e and 0.03e for carbon and chlorine atoms, respectively. Although DFT functionals such as PBE are known to overestimate charge transfer,⁴⁰ no clear evidence of such an effect can be found here since the standard deviations are of the same order of magnitude as the observed differences in the net charges. Integrated atomic dipole moments for carbon atoms are similar for the three models, with a close matching between experimental and theoretical multipolar atom models and slightly larger values for the electron density directly derived from the VASP wave function. The difference between the two theoretical models is even larger for chlorine atoms, for which a close likeness between both experimental and theoretical multipolar models is observed. Since there is a good matching between atomic charges derived from both theoretical densities, the difference in the dipole moment results from the different location of the electron distribution centroid within the atomic basin. Theoretical dipole moment values are larger for the multipolar chlorines than for those directly described from the VASP wave function because, in the latter, the electron density is more contracted around the nuclei. Indeed, as seen in the residual density maps (Figure 1), the multipolar model was not able to take into account such an atomic contraction. On the other hand, no systematic discrepancies are found between the dipole moments derived from the experimental and the theoretical multipolar models because their electron distributions are defined from the same kind of atomic functions. Moreover, as previously shown, the observed contraction of the VASP theoretically calculated electron density around chlorine atoms almost disappears when refining atomic displacement parameters, a situation that always happens with experimentally derived densities. Among the three density models, atomic quadrupolar eigenvalues of the traceless tensor differ by ~ 0.3 a.u. on average with no clear systematic tendencies.

Because the hexachlorobenzene molecule lies on an inversion center (with a half molecule in the asymmetric unit) the molecular charge and dipole moment vanish. Molecular quadrupolar moments were obtained from atomic integrated properties, combining atomic charge, dipole, and quadrupolar contributions. As seen in Table 1, large deviations occur between the three models. The theoretical models lead to different molecular quadrupolar moments mainly because their atomic dipoles are not similar (atomic charges are similar for the two models). On the other hand, experimental and theoretical multipolar models differ mainly due to the atomic charges contributions, which are larger for the latter.

The topological analyses at the bond critical points were performed by using the VMoPro software for the multipolar

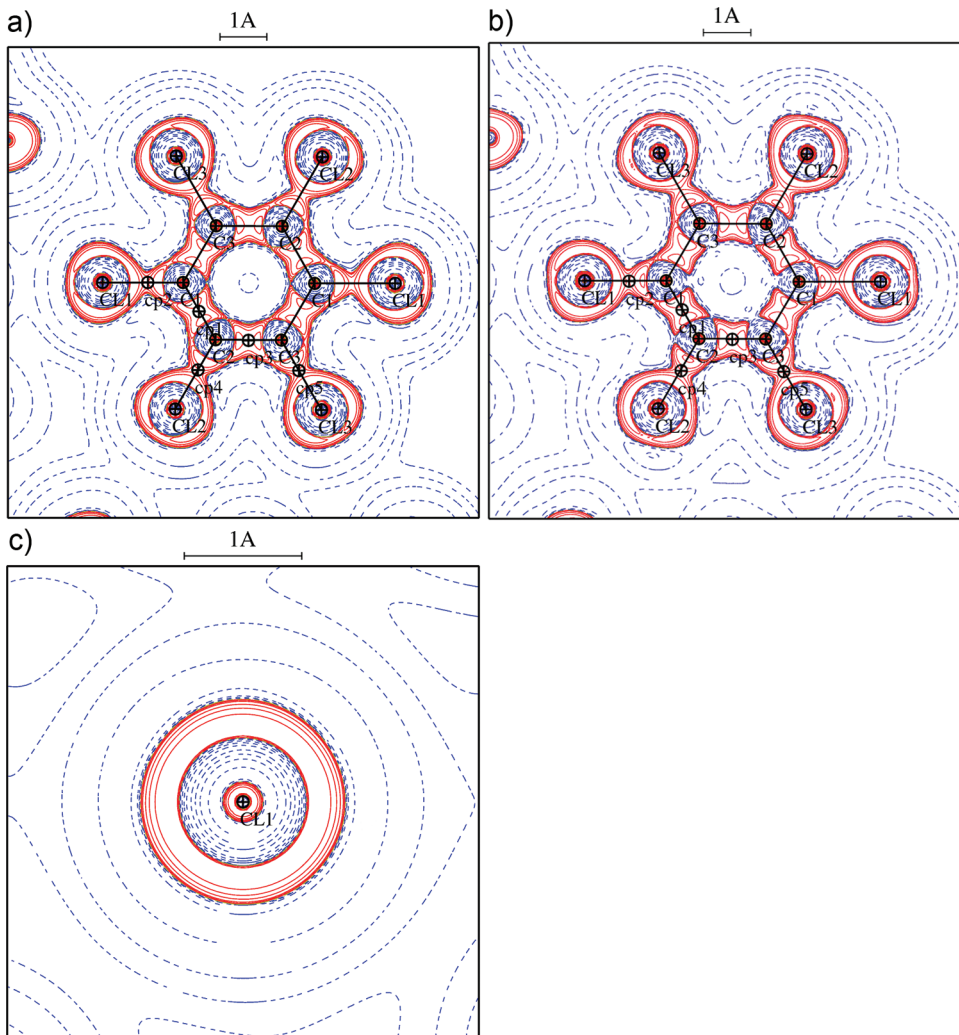


Figure 3. Laplacian maps of the total electron density: (a) theoretical and (b) experimental multipolar models within the C_6Cl_6 molecular plane, and (c) theoretical model in the perpendicular plane to the $C1-Cl1$ bond at 0.1 \AA from the $Cl1$ -nucleus, corresponding to the maximum of the deformation density at the chlorine atom. Negative contours as continuous red curves, positive contours as broken blue curves. Contours levels (in $e \cdot \text{\AA}^{-3}$) are $2, 4, 8, 0.10^n$ ($n = 0, \pm 1, \pm 2, \pm 3, \dots$).

charge densities and the Integrity program for the density directly issued from VASP (i.e., without multipolar projection). Intramolecular bond and ring critical points properties are listed in Table 2. As evidenced by previous studies comparing multipolar experimental and theoretical crystal charge densities,⁴ noticeable discrepancies are also here observed between values derived from the theoretical multipolar model and the density directly issued from VASP. These differences concern the second derivatives of the density, and are as large as $\sim 12 \text{ e} \cdot \text{\AA}^{-5}$ for $C-C$ bonds and $\sim 5 \text{ e} \cdot \text{\AA}^{-5}$ for $C-Cl$ bonds. The reason for these large differences mainly comes from the contribution of the positive curvature, which is significantly larger for the multipolar projected density. This trend parallels our previous observation of the residues on chlorine atoms (Figure 1) that we brought closer to the contraction of the electron density function in the theoretical calculation. As stated in section 3.2.2, the primary reason of this feature lies on the difference on the radial functions used in the multipolar model (Slater-type) and in the theoretical calculation (superposition of plane waves and numerical radial functions used in VASP).

The matching between the theoretical and experimental multipolar data is very good, showing a tight agreement for all derived properties. The worst result is observed for $C-C$ bonds, for which the discrepancies of the Laplacian at the bond critical point reach about 15% only. Other intramolecular second derivative bond properties (namely, the three main curvatures λ_i , $i = 1, 2, 3$) are recovered within 10%, and even within 5% for most of them. Experimental and theoretical electron density properties at critical points match within 3%, except at the ring critical point. It should be noted, however, that these very small discrepancies are systematic, the electron density and the absolute values of the laplacian being always smaller for the theoretical multipolar model than for the experimental one. Accordingly, the theoretical electron density is less concentrated at bond critical points than that derived for the experimental model, as previously shown on the deformation maps (cf. Figure 2a).

Intermolecular bond critical point properties are reported in Table 3. As for intramolecular interactions, the values of the multipolar experimental and theoretical charge densities are very close to each other. Indeed, experimental electron density and

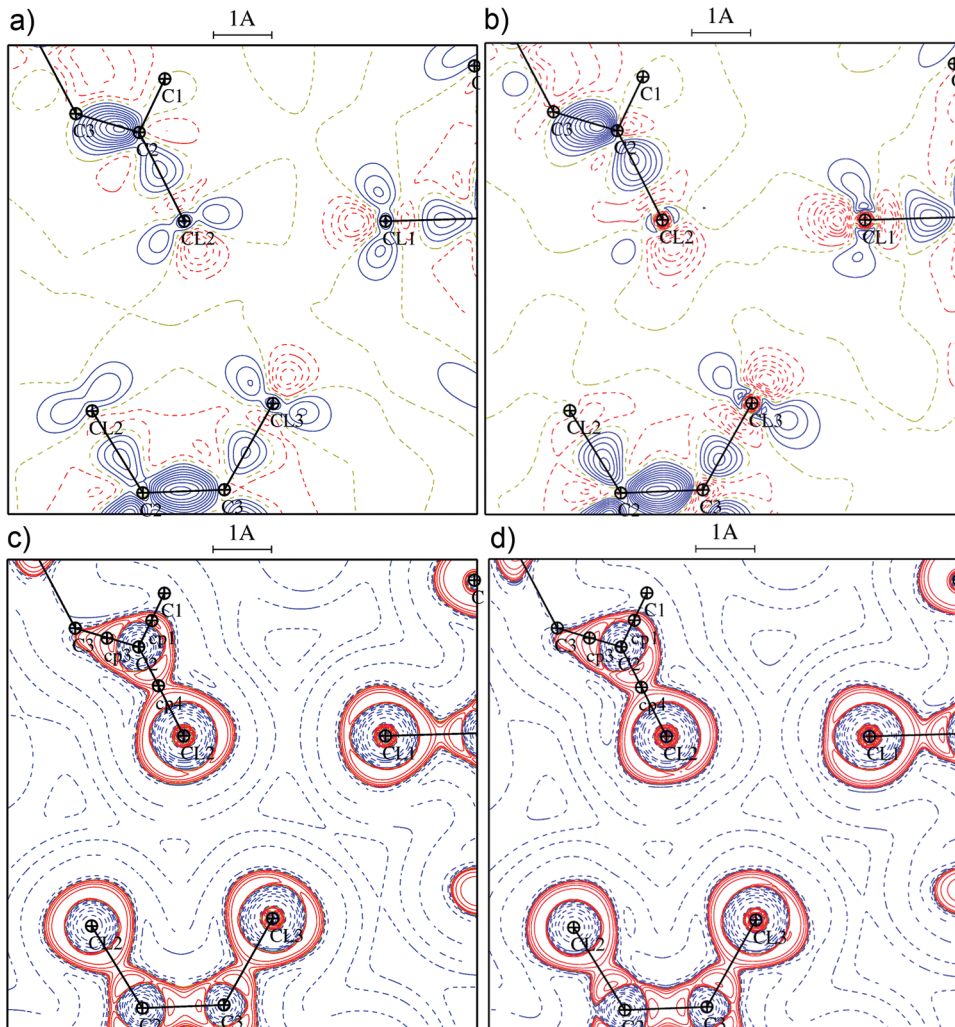


Figure 4. Static deformation density maps within the $\text{Cl}_2(x, y, z) - \text{Cl}_1(1/2 - x, 1/2 + y, 1/2 - z) - \text{Cl}_3(-1/2 - x, -1/2 + y, 1/2 - z)$ plane: (a) theoretical and (b) experimental multipolar models. Contours defined as in Figure 2a. Laplacian maps of the total electron density in the $\text{Cl}_2(x, y, z) - \text{Cl}_1(1/2 - x, 1/2 + y, 1/2 - z) - \text{Cl}_3(-1/2 - x, -1/2 + y, 1/2 - z)$ plane: (c) theoretical and (d) experimental multipolar models. Contours defined as in Figure 3.

laplacian values at intermolecular critical points differ at most 15% and 10% from the corresponding theoretical multipolar values. The observed differences are small enough to be considered lower than the experimental standard deviations associated to these quantities, which can be roughly estimated in charge density studies within $0.02 - 0.05 \text{ e} \cdot \text{\AA}^{-3}$ and $0.05 - 0.1 \text{ e} \cdot \text{\AA}^{-5}$, respectively. The very good matching between experimental and theoretical models suggests that errors on the density are lower than the previous rough estimates. As a consequence, the experimental and the theoretical multipolar models can be considered equivalent in intermolecular regions, where the matching of their derived topological properties is statistically held.

4. CONCLUSIONS

We have implemented the calculation of the structure factors in the VASP code. Periodic structure factors have been thus derived to characterize and to analyze the electron density distribution of the hexachlorobenzene molecular solid. A multipolar decomposition of $\rho(\mathbf{r})$ has been obtained from the theoretical structure factors in a condensed and simple form, which is based

on the product of Slater-type radial functions and spherical harmonics representing multipolar contributions. Such analytic electron density description has been straightforwardly used for the $\rho(\mathbf{r})$ analysis in the crystal structure of C_6Cl_6 . As shown in previous studies using different basis function types (e.g., Gaussian functions), the projection on the multipolar model has some difficulties in fully reproducing the theoretical densities, especially in what concerns the second derivatives of $\rho(\mathbf{r})$. The residual densities that are observed centered on chlorine nuclei when using the multipolar model parallel the raised difficulties. The underlying reason is certainly linked to the different type of radial functions used in the multipolar model and in the periodic theoretical calculation used to derive the electron density.

As presented in this work, the integrated and local topological properties of the theoretical multipolar model compare well with those of the experimental one: $\rho(\mathbf{r})$ properties at intra- and intermolecular critical points are reproduced within 15% (and even much better for the electron density values themselves). Some biases introduced by the multipolar model are evidenced on the atomic integrated dipole moments, while atomic quadrupoles display larger differences between experimental and theoretical models.

The comparison of the theoretically calculated and the experimentally determined multipolar $\rho(\mathbf{r})$ models presented here permits one to conclude that periodic DFT calculation done with the VASP code recovers the main features of the crystalline electron density distribution of hexachlorobenzene. In particular, the nucleophilic and electrophilic sites around the halogen nuclei, which are represented by CC and CD zones in the VSCC regions of chlorine atoms, are very well reproduced. As far as halogen bonding in hexachlorobenzene is determined by interactions involving CC and CD zones, the good agreement between the theoretical and experimental multipolar models is reflected by the matching of their electron density properties at the bond critical points in intermolecular regions. On the basis of the very good recovering of the crystalline electron density, such a study shows that periodic theoretical calculations can be potentially helpful to guide experimental studies when high quality diffraction data are difficult to obtain. This is, for example, the case of molecules involving heavier halogen atoms, such as bromine or iodine, for which X-ray absorption effects are severe when using standard laboratory sources.

■ ASSOCIATED CONTENT

5 Supporting Information. Additional residual and deformation maps are presented in the Supporting Information, along with the VASP input file (INCAR) and further details about atomic and molecular quadrupolar moments calculations. This information is available free of charge via the Internet at <http://pubs.acs.org>.

■ AUTHOR INFORMATION

Corresponding Author

*E-mail: enrique.espinosa@crm2.uhp-nancy.fr (E.E.); janos.angyan@crm2.uhp-nancy.fr (J.G.Á.).

■ ACKNOWLEDGMENT

This work has been supported by the French “Agence Nationale de la Recherche” (Grant ANR-08-BLAN-0091-01). The “Service Commun de Diffraction X” of Henri Poincaré University is thanked for providing access to Crystallographic facilities. GEN-CI-CINES (Grant 2009-X2009085106) is thanked for providing access to computing facilities. T.T.T.B. thanks the French Ministry of Research for a doctoral fellowship. Claudine Katan is thanked for fruitful discussions.

■ REFERENCES

- (1) Coppens, P. *X-ray Charge Densities and Chemical Bonding*; International Union of Crystallography Texts on Crystallography; Oxford University Press: New York, 1997.
- (2) Stewart, R. F. *J. Chem. Phys.* **1969**, *51*, 4569–4577.
- (3) Hansen, N. K.; Coppens, P. *Acta Crystallogr.* **1978**, *A34*, 909–921.
- (4) Volkov, A.; Abramov, Y.; Coppens, P.; Gatti, C. *Acta Crystallogr.* **2000**, *A56*, 332–339.
- (5) Volkov, A.; Coppens, P. *Acta Crystallogr.* **2001**, *A57*, 395–405.
- (6) Coppens, P.; Volkov, A. *Acta Crystallogr.* **2004**, *A60*, 357–364.
- (7) Koritsanszky, T.; Volkov, A.; Coppens *Acta Crystallogr.* **2002**, *A58*, 464–472.
- (8) Blöchl, P. E. *Phys. Rev. B* **1994**, *50*, 17953–17979.
- (9) Sun, G.; Kürti, J.; Rajczy, P.; Kertesz, M.; Hafner, J.; Kresse, G. *J. Mol. Struct. (THEOCHEM)* **2003**, *624*, 37–45.
- (10) Nusterer, E.; Blöchl, P. E.; Schwarz, K. *Chem. Phys. Lett.* **1996**, *253*, 448–455.
- (11) Demuth, T.; Jeanvoine, Y.; Hafner, J.; Ángyan, J. G. *J. Phys.: Condens. Matter* **1999**, *11*, 3833–3874.
- (12) Kresse, G.; Furthmüller, J. *Comput. Mater. Sci.* **1996**, *6*, 15–50.
- (13) Hafner, J. *J. Mol. Struct.* **2003**, *651*, 3–17.
- (14) Chai, J. D.; Stroud, D.; Hafner, J.; Kresse, G. *Phys. Rev. B* **2003**, *67*, 104205–104215.
- (15) Kresse, G.; Joubert, D. *Phys. Rev. B* **1999**, *59*, 1758–1775.
- (16) Bader, R. W. F. *Atoms in Molecules - A Quantum Theory*; University of Oxford Press: Oxford, 1990.
- (17) Dovesi, R.; Saunders, V. R.; Roetti, C.; Causà, M.; Harrison, N. M.; Orlando, R.; Aprà, E. Technical Report, University of Torino, 1996.
- (18) Blaha, P.; Schwarz, K.-H.; Madsen, G. K. H.; Kvasnicka, D.; Luitz, J. Technical Report, Technische Universität Wien, 1999.
- (19) Gatti, C. *Acta Crystallogr.* **1996**, *A52*, C555–C556.
- (20) Otero-de-la-Roza, A.; Blanco, M. A.; Pendás, A. M.; Luña, V. *Comput. Phys. Commun.* **2009**, *180*, 157–166.
- (21) Katan, C.; Rabiller, P.; Lecomte, C.; Guezo, M.; Oison, V.; Souhassou, M. *J. Appl. Crystallogr.* **2003**, *36*, 65–73.
- (22) Tang, W.; Sanville, E.; Henkelman, G. *J. Phys.: Condens. Matter* **2009**, *21*, 084204 <http://theory.cm.utexas.edu/vstttools/bader/>.
- (23) Yu, M.; Trinkle, D. R. *J. Chem. Phys.* **2011**, *134*, 064111–8.
- (24) Otero-de-la-Roza, A.; Luña, V. *J. Comput. Chem.* **2011**, *32*, 291–305.
- (25) Garcia, P.; Dahaoui, S.; Katan, C.; Souhassou, M.; Lecomte, C. *Faraday Discuss.* **2007**, *135*, 217–235.
- (26) Hathwar, V. R.; Guru Row, T. N. *J. Phys. Chem.* **2010**, *A114*, 13434–13441.
- (27) Bui, T. T. T.; Dahaoui, S.; Lecomte, C.; Desiraju, G. R.; Espinosa, E. *Angew. Chem., Int. Ed.* **2009**, *48*, 3838–3841.
- (28) Kresse, G.; Hafner, J. *Phys. Rev. B* **1993**, *47*, 558–561.
- (29) Kresse, G.; Hafner, J. *J. Phys. Condens. Matter* **1994**, *6*, 8245.
- (30) Kresse, G.; Furthmüller, J. *Phys. Rev. B* **1996**, *54*, 11169–11186.
- (31) Perdew, J. P.; Burke, K.; Ernzerhof, M. *Phys. Rev. Lett.* **1996**, *77*, 3865–3868.
- (32) Heyd, J.; Scuseria, G. E.; Ernzerhof, M. *J. Chem. Phys.* **2003**, *118*, 8207–8215.
- (33) Jelsch, C.; Guillot, B.; Lagoutte, A.; Lecomte, C. *J. Appl. Crystallogr.* **2005**, *38*, 38.
- (34) Guillot, B.; Viry, L.; Guillot, R.; Lecomte, C.; Jelsch, C. *J. Appl. Crystallogr.* **2001**, *34*, 214–223.
- (35) Buckingham, A. D. Basic Theory of Intermolecular Forces: Application to Small Molecules. In *Intermolecular Interactions: From Diatomics to Biopolymers*; Pullman, B., Ed.; Wiley Interscience: New York, 1978; Vol. 1, p 1.
- (36) Keith, T. A.; AIMAll, version 11.05.16; TK Gristmill Software: Overland Park, KS, 2011 (aim.tkgristmill.com).
- (37) Frisch, M. J. et al. ; Gaussian 03, revision B.05; Gaussian, Inc.: Wallingford, CT, 2004. (See Supporting Information for full reference).
- (38) Blessing, R. H. *J. Appl. Crystallogr.* **1997**, *30*, 421–426.
- (39) Svendsen, H.; Overgaard, J.; Busselez, R.; Arnaud, B.; Rabiller, P.; Kurita, A.; Nishibori, E.; Sakata, M.; Takata, M.; Iversen, B. B. *Acta Crystallogr., Sect. A* **2010**, *66*, 458–469.
- (40) Cohen, A. J.; Mori-Sánchez, P.; Yang, W. *Science* **2008**, *321*, 792–794.